TiO$_2$-Seeded Hydrothermal Growth of Spherical BaTiO$_3$ Nanocrystals for Capacitor Energy-Storage Application

Ming Li [1,2], Lulu Gu [1], Tao Li [2], Shiji Hao [2], Furui Tan [2], Deliang Chen [2,3,*], Deliang Zhu [1,*], Yongjun Xu [2], Chenghua Sun [2] and Zhenyu Yang [2,*]

[1] College of Materials Science and Engineering, Shenzhen University, Shenzhen 518060, China; 2172341493@email.szu.edu.cn (M.L.); 21611200210@email.szu.edu.cn (L.G.)

[2] School of Materials Science and Engineering, Institute of Science & Technology Innovation, Dongguan University of Technology, Dongguan 523808, China; 2016812@dgut.edu.cn (T.L.); haosj@dgut.edu.cn (S.H.); 2019126@dgut.edu.cn (F.T.); hnllxyj@dgut.edu.cn (Y.X.); chenghua.sun@monash.edu (C.S.)

[3] School of Materials Science and Engineering, Zhengzhou University, Zhengzhou 450001, China

* Correspondence: dlchen@dgut.edu.cn (D.C.); dlzhu@szu.edu.cn (D.Z.); zyyang@dgut.edu.cn (Z.Y.)

check for updates

Abstract: Simple but robust growth of spherical BaTiO$_3$ nanoparticles with uniform nanoscale sizes is of great significance for the miniaturization of BaTiO$_3$-based electron devices. This paper reports a TiO$_2$-seeded hydrothermal process to synthesize spherical BaTiO$_3$ nanoparticles with a size range of 90–100 nm using TiO$_2$ (Degussa) and Ba(NO$_3$)$_2$ as the starting materials under an alkaline (NaOH) condition. Under the optimum conditions ([NaOH] = 2.0 mol L^{-1}, $R_{Ba/Ti}$ = 2.0, T = 210 °C and t = 8 h), the spherical BaTiO$_3$ nanoparticles obtained exhibit a narrow size range of 91 ± 14 nm, and the corresponding BaTiO$_3$/polymer/Al film is of a high dielectric constant of 59, a high break strength of 102 kV mm^{-1}, and a low dielectric loss of 0.008. The TiO$_2$-seeded hydrothermal growth has been proved to be an efficient process to synthesize spherical BaTiO$_3$ nanoparticles for potential capacitor energy-storage applications.

Keywords: spherical BaTiO$_3$ nanoparticle; hydrothermal synthesis; nanoscale TiO$_2$ seed; crystal growth; dielectric property

1. Introduction

Barium titanate (BaTiO$_3$) has been an important material in the manufacture of electronic components for many years due to its unique properties of high dielectric constant, high ferroelectricity, and piezoelectricity [1–5]. BaTiO$_3$-based ceramics are of a wide range of potential applications in ferroelectric random access memory (FRAM) [6], photoelectric humidity sensors [7], solid oxide fuel cells [8], superconductors [9], ferromagnets [10,11], high capacitance capacitors [12–14], pyroelectric detectors [15], and magneto resistors [16]. Especially, tetragonal BaTiO$_3$ ceramics are widely used in multi-layer ceramic capacitors (MLCC) [17], thermistors [18], and piezoelectric sensors [19]. Conventional methods used to prepare BaTiO$_3$ ceramics are solid-state reaction processes using TiO$_2$ and BaCO$_3$ as the raw materials at an elevated temperature of more than 1200 °C. The large size and low purity of the BaTiO$_3$ ceramics obtained by the solid-state reaction have limited their applications in nanotechnological fields.

The miniaturization of electronic components and nanotechnology makes it necessary to synthesize nanometer-scale BaTiO$_3$ materials, including nanowires [20] and nanoparticles [21], with scientific appeal and technical urgency. Device miniaturization and high dielectric constant can be achieved by controlling their microstructures and compositions, which are strongly dependent on the phase,

uniformity, surface area, and size of the $BaTiO_3$ materials [22–24]. For the applications in MLCC, $BaTiO_3$ powders are usually used as dielectric fillers and blended with a polymer to a fabricate composite film with a compact and flexible surface. In order to manufacture a reliable $BaTiO_3$-based MLCC, high-quality $BaTiO_3$ powders with high purity, high crystallinity, high dispersibility, and uniform small size are the precondition. The $BaTiO_3$ fillers with a narrow particle-size distribution and suitable phases are in favor of obtaining a compact composite film with a lower content of pores, and the dense and homogeneous $BaTiO_3$ phase in polymer matrix can lead to higher dielectric properties of the composite films [25]. R.K.Goyal et al. found that the dielectric constants of the composite films filled with tetragonal $BaTiO_3$ powders are higher than those of the films with cubic $BaTiO_3$ fillers; whereas the effect of crystal phase on the dielectric losses presents an opposite trend that the composite filled with a cubic $BaTiO_3$ filler shows a lower dielectric loss than that of the tetragonal $BaTiO_3$ composite film [26]. Therefore, a high-quality $BaTiO_3$ filler is important for high performance composite dielectric films, and a recent investigation on the synthesis of $BaTiO_3$ nanocrystals via various processes has become one of the hot topics.

There have been a number of methods developed to prepare high-quality $BaTiO_3$ powders [27]. As mentioned above, the conventional route used to prepare $BaTiO_3$ powders is via a solid-state reaction between $BaCO_3$ and TiO_2 at a high temperature of 850–1400 °C [28]. This solid-state method is easy in operation and allows for mass production, but there are a number of serious drawbacks in the control of particle-size (morphology) and compositional purity. Ball-milling is usually used to mix $BaCO_3$ and TiO_2. It is not only time-consuming and labor-intensive but also easy to introduce impurities [29]. As an alternative to the solid-state process, various "wet chemical" methods, including sol-gel process [30,31], hydrothermal method [32], micro-emulsions [33], and oxalate process [34] have been developed to synthesize $BaTiO_3$ powders. These methods can produce high-purity, uniform, ultrafine $BaTiO_3$ powders. Because of the complexity of operation, multi-stage, and relatively high cost, most of these methods are mainly used at the laboratory level. It should be noted that the hydrothermal process is a promising method to synthesize $BaTiO_3$ powders with controllable morphology and chemical uniformity.

The hydrothermal method can use various processing conditions in the synthesis of $BaTiO_3$ powders including the sources of barium and titanium in an aqueous medium under crystallization or amorphous state, the hydrothermal temperature and time, and morphology-controlled agents. Because of the diversity of the factors that affect the synthesis of $BaTiO_3$ nanoparticles, hydrothermal methods are full of opportunities to improve their quality in phase composition, dimensions, and morphology. Li et al. [35] reported the synthesis of tetragonal $BaTiO_3$ nanocrystals using $TiCl_4$ (or TiO_2) as the source of titanium, $BaCl_2$ as the source of barium, and polymer(vinylpyrrolidone) (PVP) as the surfactant. Grendal et al. [36] used two titanium sources of amorphous titanium dioxide and a Ti-citrate complex solution to synthesize $BaTiO_3$ nanoparticles with a size range of 10–15 nm at different hydrothermal temperatures and times. Zhao et al. [37] used cetyltrimethylammonium bromide (CTAB), $Ba(OH)_2 \cdot 8H_2O$, and tetrabutyl titanate as the precursors to synthesize $BaTiO_3$ nanocrystals via a self-assembly process. Ozen et al. [38] reported the hydrothermal synthesis of tetragonal $BaTiO_3$ nanocrystals from a single-source amorphous barium titanate precursor in a high concentration sodium hydroxide solution via a homogeneous dissolution-precipitation reaction. From the above cases, one can see that different hydrothermal parameters and growth mechanisms can effectively adjust the formation of $BaTiO_3$ nanocrystals. In addition, a single cubic phase of $BaTiO_3$ can be formed at a low alkalinity, and a tetragonal phase of $BaTiO_3$ is easily formed under a strong alkaline condition [39].

With the motivation of preparing cubic/tetragonal $BaTiO_3$ nanocrystals with a spherical morphology, this paper herein develops a TiO_2-seeded hydrothermal process to grow $BaTiO_3$ nanocrystals using $Ba(NO_3)_2$ and TiO_2(P25) as the barium and titanium sources, respectively. This synthesis is conducted under a strong alkaline NaOH aqueous solution (pH = 13.6), and the factors that affect the formation of $BaTiO_3$ nanocrystals are systematically investigated. The major influencing factors involve molar Ba/Ti ratios, hydrothermal temperature, and hydrothermal time, and their effects

on the morphology, particle size, and phase composition of the $BaTiO_3$ nanoparticles are investigated. The possible growth mechanisms are discussed. The $BaTiO_3$/polymer/Al films containing the $BaTiO_3$ nanoparticles obtained under the optimum conditions are of a high dielectric constant of 59, a high break strength of 102 kV mm^{-1} and a low dielectric loss of 0.008. This work achieves this aim to seek optimum methods to synthesize spherical $BaTiO_3$ nanoparticles with potential applications in capacitor energy-storage and other electric devices.

2. Materials and Methods

2.1. Chemicals and Settings

Barium nitrate ($Ba(NO_3)_2$, analytical grade) was purchased from Tianjin Shengao Chemical Reagent Co., Ltd (Tianjin, China). Titanium dioxide (TiO_2, P25, chemically pure) was purchased from Degussa. Sodium hydroxide (NaOH, analytical grade) was purchased from Tianjin Komi Chemical Reagent Co., Ltd (Tianjin, China). Ethanol (analytical grade) was purchased from Tianjin Kaitong Chemical Reagent Co., Ltd (Tianjin, China). Distilled water was used in all the experiments. The drying oven (XMTD-8222) was purchased from Shanghai Jinghong Experimental Equipment Co., Ltd (Shanghai, China). The desktop high-speed centrifuge (H1850) was purchased from Hunan Xiangyi Centrifuge Co., Ltd (Xiangtan, China). The polymer (ceramic glue), a silicon-containing heat-resistant resin, was purchased from the IPINRU Chen Yu Technology Co., Ltd (Chengdu, China, Product No. CYN-01 with a curing temperature of ~220 °C). A silane coupling agent (KH550, $NH_2CH_2CH_2CH_2Si(OC_2H_5)_3$) was purchased from Guangzhou Yuantai Synthetic Material Co., Ltd (Guangzhou, China). Al foils (thickness = ~12 μm, tensile strength ≥ 180 MPa, ductility ≥ 15%) were purchased from Shenzhen Kejing Star Technology Co., Ltd (Shenzhen, China).

2.2. Growth of Spherical BaTiO$_3$ Nanoparticles

$BaTiO_3$ samples were synthesized via a hydrothermal process using TiO_2 (P25) nanoparticles as the Ti source and seeds. The synthetic process of the $BaTiO_3$ nanocrystals is shown in Figure 1. Teflon-lined autoclaves with a volume of 100 mL were used as the reaction vessel. Typically, 6.0 g of NaOH and 1.5 g of TiO_2 nanoparticles were first added into 75 mL of distilled water under magnet stirring; then a given amount of $Ba(NO_3)_2$ was added to the above suspension containing TiO_2 nanoparticles and NaOH under magnetic stirring. In the final suspensions, the molar ratios of $Ba(NO_3)_2$ to TiO_2 ($R_{Ba/Ti}$) were kept at 1.6–2.0, and the molar concentration of NaOH was about 2 mol L^{-1}. The pH values of the as-obtained suspensions before hydrothermal treatment were about 13.6. The prepared suspensions were then transferred into the Teflon-lined steel autoclaves. After carefully sealing, the autoclaves were heated in an oven at 150–210 °C for 2–16 h. After the hydrothermal reaction, the autoclaves were cooled naturally, and the solid samples were collected using a centrifugal machine (5000 rpm, 5 min), followed by washing with water for more than three times and drying at 120 °C for 24 h. The as-obtained $BaTiO_3$ solids were ground into powders using an agate mortar. These white powders, i.e., $BaTiO_3$ nanocrystals, were collected and used for characterization. The detailed processing parameters for the synthesis of $BaTiO_3$ nanocrystals are listed in Table 1. It was assumed that TiO_2 added was completely converted into $BaTiO_3$, and the theoretical mass could be calculated. The yield of $BaTiO_3$ was the ratio of the actual mass of the $BaTiO_3$ sample to their corresponding theoretical mass.
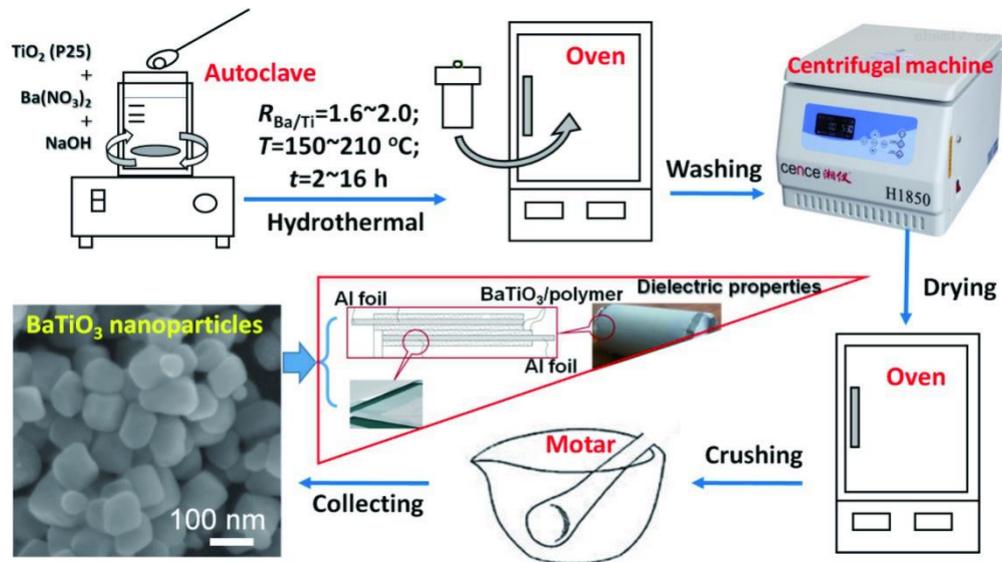
Figure 1. Schematic of the hydrothermal synthesis of BaTiO$_3$ nanocrystals using TiO$_2$ (P25) nanoparticles as the seeds and Ti source.

Table 1. A summary of experimental conditions for hydrothermal synthesis of BaTiO$_3$ nanoparticles.

Sample	[NaOH] (mol L^{-1})	$R_{Ba/Ti}$	Hydrothermal Temperature (°C)	Hydrothermal Duration (h)	Particle Size (nm)
S1	2	1.6	200	8	97 ± 15
S2	2	1.8	200	8	93 ± 24
S3	2	2.0	200	8	91 ± 22
S4	2	2.5	200	8	98 ± 26
S5	2	2.0	150	8	85 ± 15
S6	2	2.0	165	8	74 ± 13
S7	2	2.0	180	8	88 ± 10
S8	2	2.0	210	8	91 ± 14
S9	2	2.0	210	2	76 ± 17
S10	2	2.0	210	4	90 ± 15
S11	2	2.0	210	12	100 ± 20
S12	2	2.0	210	16	103 ± 20

2.3. Preparation of BaTiO$_3$/Polymer/Al (BPA) Films

To determine the possibility of the as-obtained BaTiO$_3$ nanocrystals to form a uniform film for capacitor energy-storage application, we chose sample S8 (in Table 1) as an example to prepare BaTiO$_3$/polymer/Al films (BPA films, Figure 2) using the similar method reported in our previous work [25]. Typically, the BaTiO$_3$ nanocrystals (S8) were mixed with a silicon-containing heat-resistant resin (CYN-01), and then some silane coupling agent (KH550) was added into the above mixture. Dimethylacetamide (DMAc, Guangzhou Jinhuada Chemical Reagent Co., Ltd., Guangzhou, China)) was used as the solvent. The mass ratio of M_{BaTiO3}:M_{DMAc}:$M_{Polymer}$:M_{KH550} was kept at 100:45:25:4. The as-prepared mixture was ultrasonically treated for 30 min for a uniform slurry. The above slurry was coated on an Al foil by a bar coater (T-300CA) and a coating rod (D10-OSP010-L0400) from Shijiazhuang Ospchina Machinery Technology Co., Ltd (Shijiazhuang, China)). The as-formed films were then dried in an oven at 220 °C for 10 min and finally used for the test of dielectric properties.
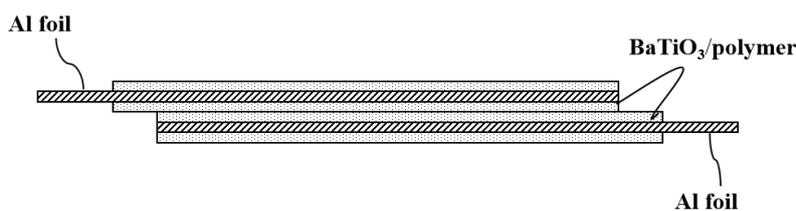
Figure 2. A schematic diagram of the BaTiO$_3$/polymer/Al film for capacitor cells.

## 2.4. Characterization of BaTiO$_3$ Nanocrystals and BPA Films

The X-ray diffraction (XRD) patterns of the BPA composite films and BaTiO$_3$ powders were recorded by a DX-2700BH X-ray diffractometer (Dandong, China) using Cu Kα irradiation. The morphologies and particle sizes of the BaTiO$_3$ samples were measured using a scanning electron microscope (SEM, Hitachi S-4800, Japan). The particle-size distribution was statistically analyzed according to the SEM images. The pH values of the suspensions were measured using a pH meter (PHS-2C). The yields of the BaTiO$_3$ samples were calculated according to the ratios of experimental BaTiO$_3$ mass to its theoretical mass on the basis of Ba conservation. Fourier-transform infrared (FT-IR) spectra were recorded on a Bruker–Equinox 55 spectrometer in a wavenumber range of 4000–400 cm^{-1} using the KBr technique. The dielectric constant (ε) and loss (tanδ) of the BPA films were measured using a high-precision high-voltage capacitor bridge (QS89, Shanghai Yanggao Capacitor Co., Ltd., Shanghai, China), and the frequency during dielectric performance test was kept at 10 Hz. The breakdown strengths of the BPA films were measured using a withstand voltage tester (GY2670A, Guangzhou Zhizhibao Electronic Instrument Co., Ltd., Guangzhou, China).

3. Results and Discussion

The TiO$_2$-seeded growth process of BaTiO$_3$ nanocrystals is shown in Figure 1. The commercially available TiO$_2$ (P25) nanoparticles, with a mixed phase of anatase and rutile and a size range of 20–25 nm, are used as the Ti source and seeds in the synthesis of BaTiO$_3$ nanocrystals via a conventional hydrothermal process in a strongly basic aqueous solution. In this synthesis, TiO$_2$ nanoparticles can first react with NaOH and form insoluble titanate species (e.g., Na$_2$TiO$_3$), which then act like the crystal nucleus to form BaTiO$_3$ nanocrystals by reacting with Ba^{2+} ions under the hydrothermal conditions. We systematically investigated the effects of molar ratios of Ba/Ti ($R_{Ba/Ti}$), hydrothermal temperature (T/°C) and time (t/h) on the phase, morphology and particle size of the BaTiO$_3$ nanocrystals.

3.1. Influence of Molar Ba/Ti Ratio

In order to verify the effect of the molar Ba/Ti ratio on the formation of BaTiO$_3$ nanoparticles, we synthesized a series of samples with various $R_{Ba/Ti}$ values from 1.6 to 2.5, and the other hydrothermal conditions were kept as the same: sodium hydroxide concentration [NaOH] = 2.0 mol L^{-1} (pH = 13.6), T = 200 °C, and t = 8 h. The typical results of these samples are shown in Figure 3.
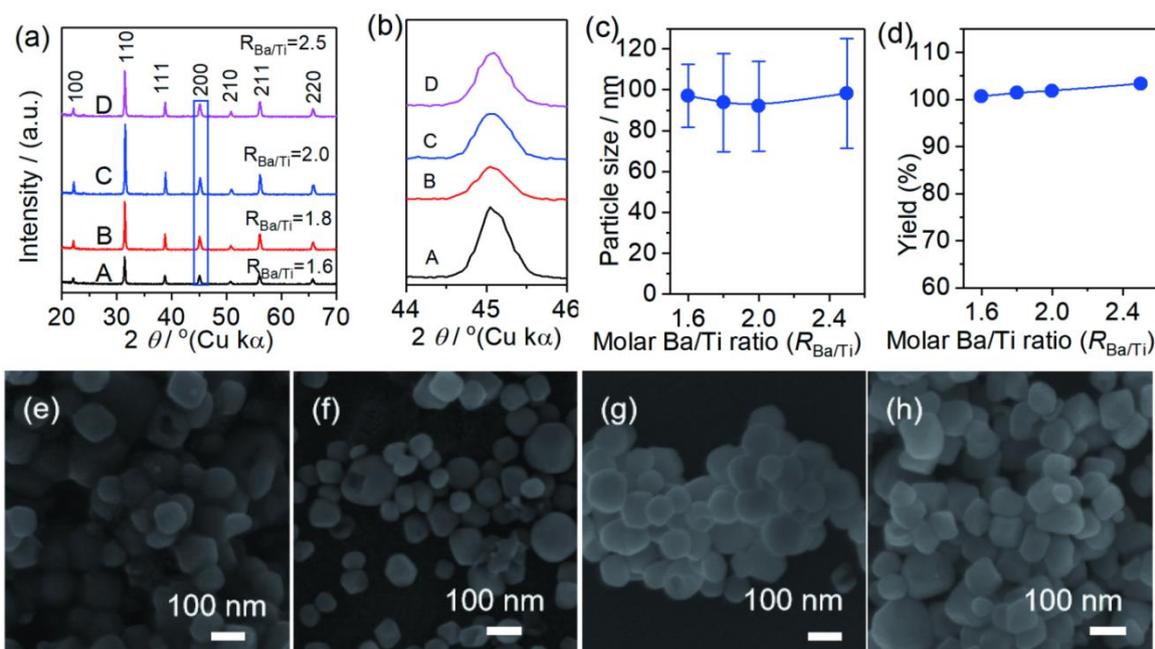
Figure 3. X-ray diffraction (XRD) patterns (**a**,**b**), particle sizes and yields (**c**,**d**), and scanning electron microscope (SEM) images (**e**–**h**) of the $BaTiO_3$ samples obtained with various molar Ba/Ti ratios ($R_{Ba/Ti}$ = 1.6–2.5) under hydrothermal conditions at 200 °C for 8 h ([NaOH] = 2.0 mol L^{-1}, pH ≈ 13.6).

Figure 3a,b shows the XRD patterns of the $BaTiO_3$ samples synthesized at different molar Ba/Ti ratios. From Figure 3a, one can find that all the samples show seven distinct peaks at around 21.98, 31.36, 38.64, 44.92, 50.58, 55.86 and 65.44°, corresponding to the (100), (110), (111), (200), (210), (211) and (220) reflections of the cubic $BaTiO_3$ phase, respectively, according to the JCPDS card no. 31-0174 [40]. No peaks belonging to other identifiable impurities can be found in all the samples obtained, indicating the as-obtained $BaTiO_3$ samples are pure. As Figure 3b shows, the peak at about 45° can be divided into two diffraction sub-peaks at 44.9 and 45.3°, attributable to the (200) and (002) reflections of the tetragonal $BaTiO_3$ species, respectively [41]. With the increase of the $R_{Ba/Ti}$ value from 1.6 to 2.5, the peaks near 45° become wider and wider, suggesting that a higher $R_{Ba/Ti}$ value is favorable in forming a tetragonal $BaTiO_3$ phase.

Figure 3c shows the plots of particle size dependent on the $R_{Ba/Ti}$ values. When $R_{Ba/Ti}$ = 1.6–1.8, the particle sizes are 90–100 nm (97 ± 15 nm for $R_{Ba/Ti}$ = 1.6 and 93 ± 24 nm for $R_{Ba/Ti}$ = 1.8), but the uniform degree is not high. Figure 3d shows the yields of $BaTiO_3$ samples synthesized with various $R_{Ba/Ti}$ values after hydrothermally treating at 200 °C for 8 h ([NaOH] = 2.0 mol L^{-1}). One can see that the yields of all the samples are close to 100%, indicating the complete conversion of TiO_2 to $BaTiO_3$ nanocrystals. The formation of a small amount of crystal water may make the $BaTiO_3$ yield a little larger than 100% according to the TiO_2 amount [42].

Figure 3e–h shows the typical SEM images of the $BaTiO_3$ samples obtained with various $R_{Ba/Ti}$ values ([NaOH] = 2.0 mol L^{-1}, T = 200 °C, t = 8 h). According to the SEM observations, when $R_{Ba/Ti}$ = 2.0 (Figure 3g), the particle size of the $BaTiO_3$ sample is 91 ± 22 nm, and it shows a more uniform solid spherical particle morphology. When $R_{Ba/Ti}$ = 2.5 (Figure 3h), the particle size of the $BaTiO_3$ sample is 98 ± 26 nm, and one can see that it shows obviously clean-cut crystal faces for the $BaTiO_3$ particles, suggesting a higher degree of crystallinity and favorable formation of the tetragonal $BaTiO_3$ phase.

Taking the results of XRD and particle-size distribution into account, we can tentatively conclude that a higher Ba/Ti ratio is more favorable in forming tetragonal $BaTiO_3$ nanocrystals with a more uniform size.

3.2. Influence of Hydrothermal Temperature

The effect of hydrothermal temperature on the synthesis of $BaTiO_3$ nanoparticles was investigated by changing the hydrothermal temperature from 150 to 210 °C under the conditions: $R_{Ba/Ti} = 2.0$, $t = 8$ h and $[NaOH] = 2.0$ mol L^{-1}, and Figure 4 shows their characterization results of XRD and SEM.
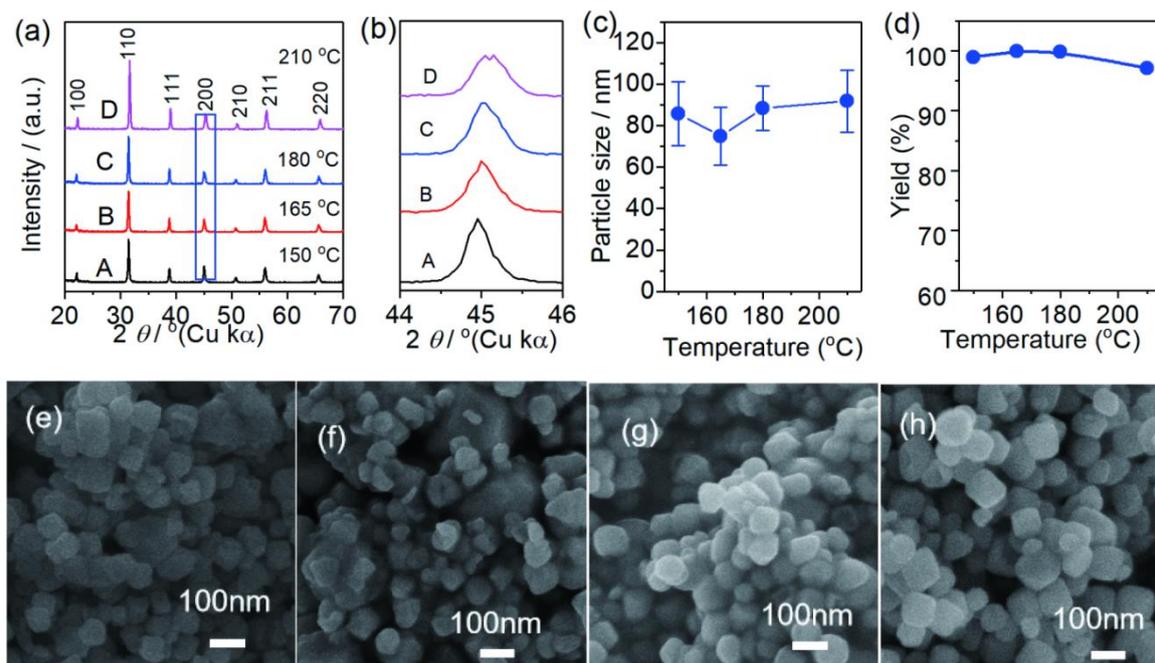
Figure 4. XRD patterns (**a**,**b**), particle sizes and yields (**c**,**d**), and SEM images (**e**–**h**) of the $BaTiO_3$ nanocrystals obtained with $R_{Ba/Ti} = 2.0$ under hydrothermal conditions at 150–210 °C for 8 h ($[NaOH] = 2.0$ mol L^{-1}, pH ≈ 13.6).

Figure 4a,b shows the typical XRD patterns of the $BaTiO_3$ samples obtained at different hydrothermal temperatures. From Figure 4a, one can see that all the $BaTiO_3$ samples show similar XRD patterns, all peaks of which can be attributed to the cubic $BaTiO_3$ phase (JCPDS card no. 31-0174), and no impure XRD peaks are found, indicating that the formation of pure $BaTiO_3$ crystals. The partially enlarged XRD patterns located in $2\theta = 44$–46° (Figure 4b) show the XRD peaks become wider and wider with the increase of hydrothermal temperature from 150 to 210 °C, and can be sub-divided to two peaks at 44.9° and 45.3°, attributable to the (200) and (002) reflections of the tetragonal $BaTiO_3$ phase.

Figure 4c shows the particle-size distribution plot versus hydrothermal temperature (T). When $T = 150$ °C, the particle sizes of the as-obtained $BaTiO_3$ nanocrystals are 85 ± 15 nm. When $T = 165$ °C, the particle size of the as-obtained $BaTiO_3$ is about 74 ± 13 nm, seeming to become smaller, but their uniformity is low. When the temperature increases to 180 °C, the particle size of the as-obtained $BaTiO_3$ is 88 ± 10 nm, and the morphology of the $BaTiO_3$ particles becomes relatively uniform. When $T = 210$ °C, the particle size of the as-obtained the $BaTiO_3$ sample is 91 ± 14 nm, just a slight increase. As Figure 4c shows, the particle sizes of the $BaTiO_3$ samples obtained at various hydrothermal temperatures are kept almost constant at about 80–90 nm.

Figure 4d shows the plot of the yield of the $BaTiO_3$ sample versus the hydrothermal temperature. One can see that during the hydrothermal temperature of 150–180 °C, the yield is close to 100%; when the hydrothermal temperature is 210 °C, the yield slightly decreases because of the complete dehydration reaction in the elevated temperature.

Figure 4e–h shows the typical SEM images of the $BaTiO_3$ samples synthesized under various hydrothermal temperatures for 8 h ($[NaOH] = 2.0$ mol L^{-1}, $R_{Ba/Ti} = 2.0$): (e) 150 °C, (f) 165 °C, (g) 180 °C, and (h) 210 °C. One can see that all the $BaTiO_3$ samples consist of spherical nanoparticles. With

the increase of hydrothermal temperature, the as-obtained $BaTiO_3$ samples exhibit a higher degree of crystallinity indicated by the clean-cut crystal planes.

According to the XRD patterns (Figure 4a,b) and SEM images (Figure 4e–h), we find that a higher hydrothermal temperature is helpful to form tetragonal $BaTiO_3$ nanocrystals with more uniform spherical morphology. For safety's sake, the hydrothermal temperature is chosen as 210 °C for the synthesis of $BaTiO_3$ nanocrystals in the following investigation. Cautions: the working temperature limit of a PTFE hydrothermal reactor is usually about 220 °C, and a too high temperature will cause explosion.

3.3. Influence of Hydrothermal Time

The effect of hydrothermal time on the formation of $BaTiO_3$ nanocrystals (Figure 5) are investigated under the conditions: $R_{Ba/Ti}$ = 2.0, T = 210 °C, [NaOH] = 2.0 mol L^{-1}, and t = 2–16 h. Figure 5a,b shows their XRD patterns. As Figure 5a shows, the XRD peaks of all the samples can be assignable to the cubic/tetragonal $BaTiO_3$ phase with no other identifiable impurity peaks. The partially enlarged XRD patterns in Figure 5b shows the details that the XRD peaks at around 45° become wider and wider as the hydrothermal time increases from 2 h to 16 h, indicating that the $BaTiO_3$ sample obtained with a longer hydrothermal time has more tetragonal $BaTiO_3$ species.
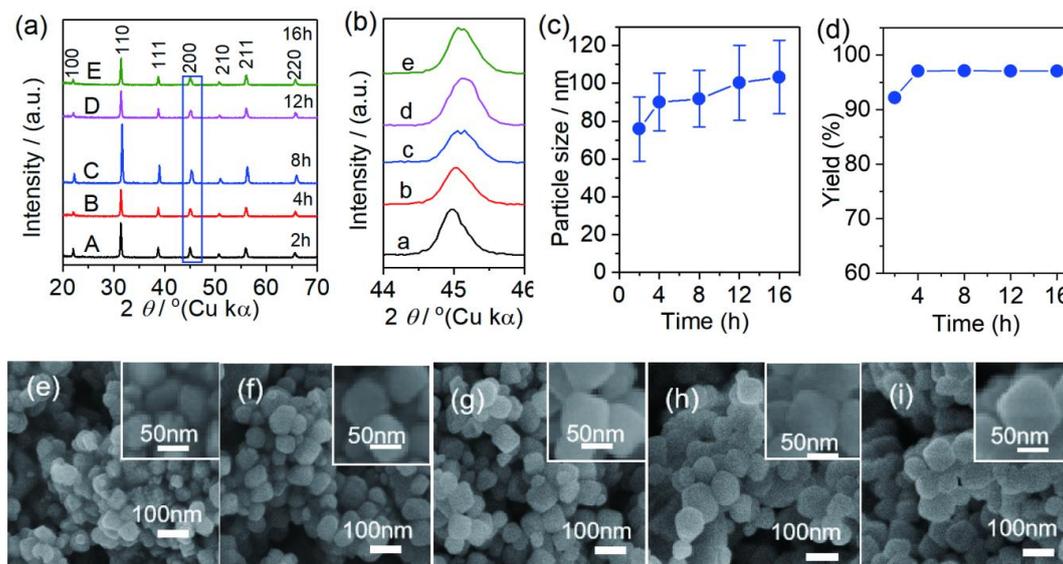

Figure 5. XRD patterns (**a,b**), particle sizes and yields (**c,d**), and SEM images (**e–i**) of the $BaTiO_3$ nanocrystals obtained with $R_{Ba/Ti}$ = 2.0([NaOH]=2.0 mol L^{-1}, pH ≈ 13.6) by hydrothermally treating at 210 °C for various times (t = 2–16 h).

Figure 5c shows the $BaTiO_3$ sample gradually changes from small nanoparticles (~70 nm) to large ones (~100 nm) as the hydrothermal time is prolonged from 2 h to 16 h. Figure 5d shows the yield plot of the $BaTiO_3$ nanocrystals versus hydrothermal time. With a short hydrothermal time of 2 h, the $BaTiO_3$ yield is about 92% because of the incomplete reaction. When the hydrothermal time increases to 4–16 h, the yields of the $BaTiO_3$ samples is close to 98%.

Figure 5e–h shows the SEM images of the $BaTiO_3$ samples obtained with various hydrothermal times ($R_{Ba/Ti}$ = 2.0, T = 210 °C, [NaOH] = 2.0 mol L^{-1}). The $BaTiO_3$ samples obtained with short hydrothermal times of 2–8 h, as shown in Figure 5e–g, exhibit a spherical shape; when the hydrothermal time increases to 12–16 h, as Figure 5h,i shows, the as-obtained $BaTiO_3$ samples take on a planar polyhedral morphology. It is interesting that the particle sizes of the $BaTiO_3$ samples are close to 100 nm and not changed obviously with the prolonging of hydrothermal time to 16 h. In addition, as

Figure 5i shows, the BaTiO$_3$ nanoparticles obtained by hydrothermal treating at 210 °C for 16 h are uniform in particle size and well dispersed.

Figure 6 shows the FT-IR spectra of the BaTiO$_3$ samples synthesized with different hydrothermal times ($R_{Ba/Ti}$ = 2.0, T = 210 °C, [NaOH] = 2.0 mol L^{-1}). The bands at 3431 and 1568 cm^{-1} can be attributed to the stretching mode of the adsorbed water molecules and O–H groups, indicating that the surfaces of the BaTiO$_3$ nanocrystals contain some adsorbed water and –OH groups. The weak band at 1400 cm^{-1} can be attributed to the stretching mode of the C–O groups because of the incorporation of CO$_2$ into the basic solution. The broad and strong absorption bands at 562 cm^{-1} is attributed to the normal vibration of Ti–O$_{I}$ stretching, and the weaker and sharper absorption bands near 438 cm^{-1} can be attributed to the normal vibration of Ti–O$_{II}$ bending. When the hydrothermal time is extended from 2 h to 16 h, the bands at 562 and 438 cm^{-1} become stronger and sharper, indicating that the BaTiO$_3$ nanocrystals with a high degree of crystallinity are formed. According to the XRD patterns (Figure 5a,b), SEM images (Figure 5e–i) and FT-IR spectra (Figure 6), the BaTiO$_3$ nanocrystals obtained by hydrothermal treating at 210 °C for more than 8 h are of uniform spherical morphologies with a size range of 95–100 nm and high degree of crystallinity. Therefore, the optimum hydrothermal parameters for the synthesis of BaTiO$_3$ nanocrystals can be $R_{Ba/Ti} \geq 2$, $T \geq 200$ °C, $t \geq 8$ h. The as-obtained BaTiO$_3$ nanocrystals are of a mixture of cubic and tetragonal phases and exhibit a uniform spherical particulate morphology with a size range of 90–100 nm. The as-obtained spherical BaTiO$_3$ nanocrystals show a high performance in ceramic capacitor for energy-storage applications.
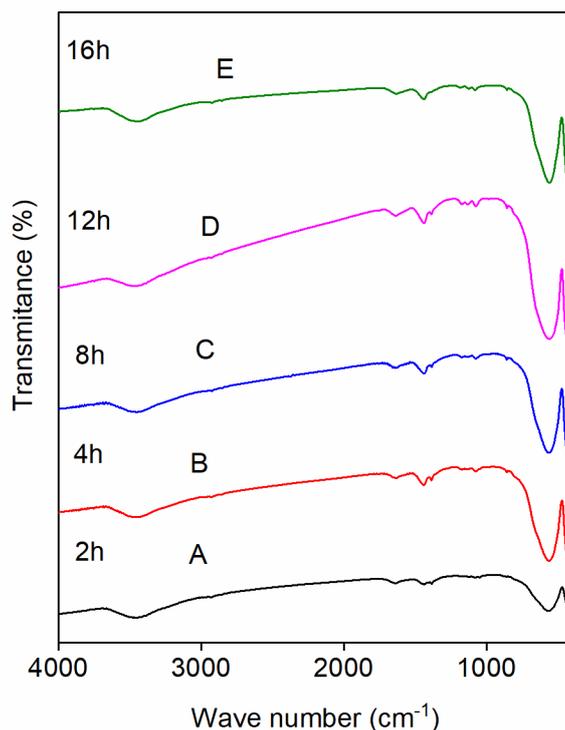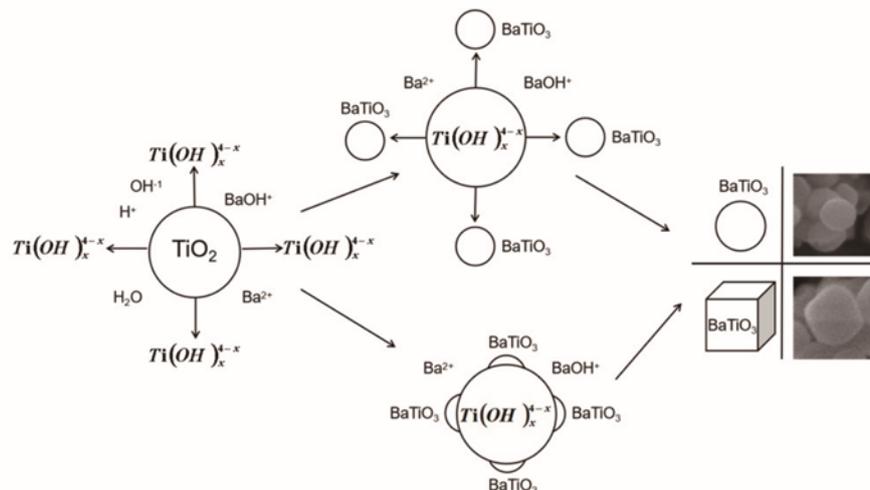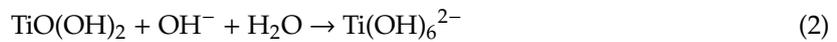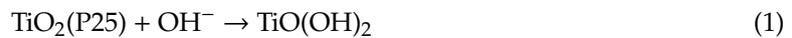

Figure 6. Typical FT-IR spectra of the BaTiO$_3$ nanocrystals obtained by hydrothermally treating at 210 °C for various times (2–16 h) with $R_{Ba/Ti}$ = 2.0 and [NaOH] = 2.0 mol L^{-1}.

3.4. Understanding of Growth Mechanism

In the hydrothermal synthesis of BaTiO$_3$ nanocrystals, TiO$_2$ (P25) nanoparticles are used as the solid-state Ti source and seeds for crystal growth. The possible growth mechanism of the BaTiO$_3$ nanocrystals by the hydrothermal process is shown in Figure 7. TiO$_2$ nanoparticles first react with OH$^-$ ions in a strong alkaline solution to form a soluble titanium hydroxide complex, which can form a negatively charged Ti–O chain. These negatively charged Ti–O chains attract positively charged Ba^{2+}

or BaOH$^+$ ions to form BaTiO$_3$ nuclei, on which the excess Ba^{2+} species continue to grow in the strong alkaline solution under the hydrothermal conditions for a long time. The possible reactions for the growth of BaTiO$_3$ nanocrystals can be described as follows:

$$TiO_2(P25) + OH^- \rightarrow TiO(OH)_2 \tag{1}$$

$$TiO(OH)_2 + OH^- + H_2O \rightarrow Ti(OH)_6^{2-} \tag{2}$$

$$Ti(OH)_6^{2-} + Ba^+ \rightarrow BaTiO_3 + H_2O \tag{3}$$

Figure 7. Possible growth mechanism for the synthesis of BaTiO$_3$ nanocrystals under the hydrothermal conditions using TiO$_2$ nanoparticles (P25) as the seeds and Ti source.

Using TiO$_2$ (P25) nanoparticles as the seeds and Ti source for the synthesis of BaTiO$_3$ nanocrystals, the negatively charged Ti–O chains are first formed on the surface of TiO$_2$ (P25) particles in the strong alkaline solution, and the whole TiO$_2$ (P25) nanoparticles are then gradually transformed to the [Ti(OH)$_x$]$^{4-x}$ species. The negatively charged Ti–O chains (i.e., [Ti(OH)$_6$]$^{2-}$) react with Ba^{2+} ions to form BaTiO$_3$ nanocrystals under hydrothermal conditions. The large spherical particles in situ formed on the TiO$_2$ (P25) nuclei may overcome the agglomeration because of their weak attraction to each other. The small particles can be self-regulated by the interaction of van der Waals torque (Casimir Torque) under high-temperature Brownian motion via the orientation attachment mechanism [43]. During the long hydrothermal reaction, smaller crystals dissolve and re-deposit on larger particles for orientation attachment and crystal extension via the Ostwald ripening process. Therefore, the growth mechanism for the formation of BaTiO$_3$ nanoparticles may involve the following steps: (1) TiO$_2$ (P25) nanoparticles are transformed to [Ti(OH)$_x$]$^{4-x}$ species in the strong alkaline solution; (2) Ba^{2+} ions reacts with [Ti(OH)$_x$]$^{4-x}$ species to form BaTiO$_3$ nanocrystals; (3) small BaTiO$_3$ nanocrystals grows to large ones via the Ostwald ripening process and the orientation attachment mechanism.

3.5. Dielectric Properties of the BPA Film with BaTiO$_3$ Nanoparticles

The spherical BaTiO$_3$ nanoparticles with a size range of 91 ± 14 nm (S8 in Table 1) obtained under the optimum conditions ([NaOH] = 2.0 mol L^{-1}, $R_{Ba/Ti}$ = 2.0, T = 210 °C and t = 8 h) were used to prepare BaTiO$_3$/polymer/Al (BPA) composite films to verify the feasibility of the BaTiO$_3$ sample in capacitor energy-storage applications.

The typical XRD patterns, SEM image and dielectric properties of the typical BPA films with the BaTiO$_3$ sample (S8) are shown in Figure 8. Figure 8a shows the XRD patterns of the BaTiO$_3$ sample, polymer/Al foil, and BPA film. According to the JCPDS card (No. 99-0005), the diffraction peaks at

$2\theta = 38.47°$, $44.72°$, and $65.09°$ correspond to the (111), (200), and (220) of the Al foil, respectively. The XRD pattern of the BPA film is a superposition of the $BaTiO_3$ sample and Al foil, and no other impurities are found in the BPA film. Figure 8b shows a typical SEM image of the BPA film. The film exhibits a uniform distribution of $BaTiO_3$ nanoparticles. Figure 8c gives the dielectric properties of the BPA films with spherical $BaTiO_3$ nanoparticles. As the statistical results show, the average dielectric constant of the BPA films reaches 59, the average dielectric loss reaches 0.008, and the average breakdown strength reaches 102 kV mm^{-1}. These electrical properties are much higher than those of the previous reports [44–49]. The TiO_2-seeded hydrothermal process is an efficient process to synthesize spherical $BaTiO_3$ nanoparticles for potential capacitor energy-storage applications.
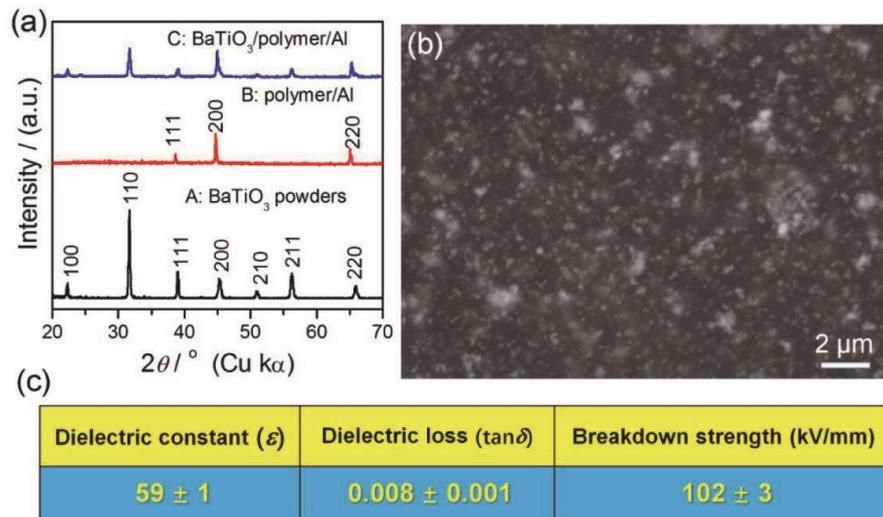
Figure 8. XRD, SEM, and dielectric properties of the typical $BaTiO_3$/polymer/Al films (BPA) films with $BaTiO_3$ nanocrystals (S8): (**a**) XRD patterns (A-BaTiO3 nanocrystals, B-Polymer/Al film and (C)-BaTiO$_3$/polymer/Al (BPA) film); (**b**) the typical SEM image of the BPA film; (**c**) typical electric properties of the BPA films.

We compared the dielectric constant, dielectric loss, and breakdown strength of the BPA films with those of the literature reports [25,31,44,46,49,50], and the results are shown in Table 2. One can find that the BPA films with the TiO_2-seeded $BaTiO_3$ nanocrystals exhibit an excellent balanced dielectric performance.

Table 2. Comparisons of dielectric constant, dielectric loss and breakdown strength of the composites containing BT particles.

Fillers	Polymer Matrix	Dielectric Constant	Break Strength	Dielectric Loss	Reference
BT microparticles	Resin	32	20.8 V/μm	0.014	[25]
BT microparticles	Resorcinol and formaldehyde	16.6	/	0.019	[31]
PDA coated BT nanoparticles (100 nm)/BN nanosheets	Poly(vinylidene fluoride -chlorotrifluoroethylene)	11.7	425 MV/m	0.10	[44]
Sphere-like TiO_2 nanowire clusters	Poly(vinylidene fluoride-co -hexafluoropylene)	11.9	160 kV/mm	0.048	[46]
$CaCu_3Ti_4O_{12}$@TiO_2 nanofibers	In suit prepared polyimide	5.85	236 kV/mm	0.025	[49]
PVP coated BT nanoparticles (100 nm)	Poly(vinylidene fluoride)	80.4	240 kV/mm	0.085	[50]
BT microparticles	Resin	59	102 kV/mm	0.008	This work

4. Conclusions

TiO$_2$ (P25) nanoparticle assisted hydrothermal process has been developed to synthesize BaTiO$_3$ nanocrystals in a strong alkaline solution (pH = 13.6) using TiO$_2$ (P25) and Ba(NO$_3$)$_2$ as the starting materials and NaOH as the mineralizer. The particle sizes, morphologies, and phases of the BaTiO$_3$ nanocrystals have been controlled by changing the molar Ba/Ti ratio, the hydrothermal temperature, and time. The XRD and SEM results indicate that a high Ba/Ti ratio (≥2.0), a high hydrothermal temperature (≥200 °C), and a long hydrothermal time (≥8 h) are favorable in forming a mixture of cubic/tetragonal BaTiO$_3$ nanocrystals with a uniform, well-dispersed spherical particulate morphology (90–100 nm). Under the optimum conditions ([NaOH] = 2.0 mol L^{-1}, $R_{Ba/Ti}$ = 2.0, T = 210 °C and t = 8 h), the as-obtained spherical BaTiO$_3$ nanoparticles have a narrow particle size range of 91 ± 14 nm. It should be emphasized that the particle size and morphology of the BaTiO$_3$ nanocrystals are kept relatively stable when the hydrothermal conditions change in a proper range, suggestive of a robust and efficient process toward spherical BaTiO$_3$ nanocrystals. The growth mechanism of the TiO$_2$-assisted hydrothermal process for the synthesis of BaTiO$_3$ nanocrystals has been attributed to the dissolution-crystallization, Oswald ripening, and oriented attachment process. The BaTiO$_3$/polymer/Al films containing the above BaTiO$_3$ nanoparticles are of a high dielectric constant of 59, a high break strength of 102 kV mm^{-1}, and a low dielectric loss of 0.008. The TiO$_2$-seeded hydrothermal process developed here is an efficient process to synthesize spherical BaTiO$_3$ nanoparticles for potential capacitor energy-storage applications.

References

1. Wang, C.; Yan, F.; Yang, H.; Yin, Y.; Wang, T. Dielectric and ferroelectric properties of SrTiO$_3$-Bi$_{0.54}$Na$_{0.46}$TiO$_3$-BaTiO$_3$ lead-free ceramics for high energy storage applications. *J. Alloys Compd.* **2018**, *749*, 605–611. [CrossRef]

2. Si, F.; Tang, B.; Fang, Z.X.; Li, H.; Zhang, S.R. A new type of BaTiO$_3$-based ceramics with Bi(Mg$_{1/2}$Sn$_{1/2}$)O$_3$ modification showing improved energy storage properties and pulsed discharging performances. *J. Alloys Compd.* **2020**, *819*, 153004. [CrossRef]

3. Liu, S.N.; Liu, C.C.; You, Y.; Wang, Y.J.; Wei, R.B. Fabrication of BaTiO$_3$-Loaded Graphene Nanosheets-Based Polyarylene Ether Nitrile Nanocomposites with Enhanced Dielectric and Crystallization Properties. *Nanomaterials* **2019**, *9*, 9121667. [CrossRef] [PubMed]

4. Li, Y.H.; Wu, J.; Wu, X.D.; Suo, H.; Shen, X.D.; Cui, S. Synthesis of bulk BaTiO$_3$ aerogel and characterization of photocatalytic properties. *J. Sol-Gel Sci. Technol.* **2019**, *90*, 313–322. [CrossRef]

5. Song, R.X.; Zhao, Y.; Li, W.L.; Yu, Y.; Sheng, J.; Li, Z.; Zhang, Y.L.; Xia, H.T.; Fei, W.D. High temperature stability and mechanical quality factor of donor-acceptor co-doped BaTiO$_3$ piezoelectrics. *Acta Mater.* **2019**, *181*, 200–206. [CrossRef]

6. Meeker, M.A.; Kundu, S.; Mauryn, D.; Kang, M.; Sosa, A.; Mudiyanselage, R.H.; Clavel, M.; Gollapudit, S.; Hudait, M.K.; Priya, S.; et al. The permittivity and refractive index measurements of doped barium titanate (BT-BCN). *Opt. Mater.* **2017**, *73*, 793–798. [CrossRef]

7.   Sikarwar, S.; Sonker, R.K.; Shukla, A.; Yadav, B.C. Synthesis and investigation of cubical shaped barium titanate and its application as opto-electronic humidity sensor. *J. Mater. Sci.-Mater. Electron.* **2018**, *29*, 12951–12958. [CrossRef]

8.   Hapani, D.S.; Singh, P.; Jha, P.K.; Singh, P. A comparative electrical conductivity behavior of $BaTiO_3$ and $CaTiO_3$ ceramics. *AIP Conf. Proc.* **2018**, *2009*, 020010.

9.   Kabanov, V.V.; Piyanzina, I.I.; Tayurskii, D.A.; Mamin, R.F. Towards high-temperature quasi-two-dimensional superconductivity. *Phys. Rev. B* **2018**, *98*, 094522. [CrossRef]

10. Sasikumar, S.; Thirumalaisamy, T.K.; Saravanakumar, S.; Sivaganesh, D. Effect of neodymium doping in $BaTiO_3$ ceramics on structural and ferroelectric properties. *J. Mater. Sci.-Mater. Electron.* **2019**, *19*, 02670. [CrossRef]

11. Abdullah-Al, M.M.; Haque, A.; Pelton, A.; Paul, B.; Ghosh, K. Structural, electronic, and magnetic analysis and device characterization of ferroelectric-ferromagnetic heterostructure (BZT-BCT/LSMO/LAO) devices for multiferroic applications. *IEEE Trans. Magn.* **2018**, *54*, 2502908.

12. Akram, F.; Kim, J.C.; Khan, S.A.; Zeb, A.; Yeo, H.G.; Sung, Y.S.; Song, T.K.; Lee, S. Less temperature-dependent high dielectric and energy-storage properties of eco-friendly $BiFeO_3$-$BaTiO_3$-based ceramics. *J. Alloys Compd.* **2020**, *818*, 152878. [CrossRef]

13. Wang, H.X.; Liu, B.B.; Wang, X.H. Effects of dielectric thickness on energy storage properties of surface modified $BaTiO_3$ multilayer ceramic capacitors. *J. Alloys Compd.* **2020**, *817*, 152804. [CrossRef]

14. Park, H.; Na, Y.; Choi, H.J.; Suh, S.; Baek, D.H.; Yoon, J.R. Electrical properties of $BaTiO_3$-based 0603/0.1 µF/0.3 mm ceramics decoupling capacitor for embedding in the PCB of 10G RF transceiver module. *J. Electr. Eng. Technol.* **2018**, *13*, 1637–1642.

15. Ianculescu, A.; Pintilie, I.; Vasilescu, C.A.; Botea, M.; Iuga, A.; Melinescu, A.; Dragan, N.; Pintilie, L. Intrinsic pyroelectric properties of thick, coarse grained $Ba_{1-x}Sr_xTiO_3$ ceramics. *Ceram. Int.* **2016**, *42*, 10338–10348. [CrossRef]

16. Wang, J.; Bai, J.; Jin, Z.; Chen, C.; Zhai, W. Temperature dependent magnetoelectric coupling in $BaTiO_3$/$La_{0.67}Sr_{0.33}MnO_3$ heterojunction. *J. Phys. D Appl. Phys.* **2018**, *51*, 135305. [CrossRef]

17. Hong, K.; Lee, T.H.; Suh, J.M.; Park, J.S.; Kwon, H.S.; Choi, J.; Jang, H.W. Direct observation of surface potential distribution in insulation resistance degraded acceptor-doped $BaTiO_3$ multilayered ceramic capacitors. *Electron. Mater. Lett.* **2018**, *14*, 629–635. [CrossRef]

18. Kim, J. Electrical and thermal properties of a $(Ba_{1-x-y}Sr_xCa_y)TiO_3$-based PTC thermistor for preheating light oil. *Funct. Mater. Lett.* **2018**, *11*, 1850076. [CrossRef]

19. Cernea, M.; Vasile, B.S.; Surdu, V.A.; Trusca, R.; Bartha, C.; Craciun, F.; Galassi, C. Electric and magnetic properties of ferromagnetic/piezoelectric bilayered composite. *J. Mater. Sci.* **2018**, *53*, 14160–14171. [CrossRef]

20. Wu, J.; Qin, N.; Yuan, B.; Lin, E.; Bao, D. Enhanced pyroelectric catalysis of $BaTiO_3$ nanowires for utilizing waste heat in pollution treatment. *ACS Appl. Mater. Interfaces* **2018**, *10*, 37963–37973. [CrossRef]

21. Jin, M.H.; Shin, E.; Jin, S.; Jo, H.; Ok, K.M.; Hong, J.; Jun, B.H.; Durrant, J.R. Solvothermal synthesis of ferroelectric $BaTiO_3$ nanoparticles and their application to dye-sensitized solar cells. *J. Korean Phys. Soc.* **2018**, *73*, 627–631. [CrossRef]

22. Schadli, G.N.; Buchel, R.; Pratsinis, S.E. Nanogenerator power output: Influence of particle size and crystallinity of $BaTiO_3$. *Nanotechnology* **2017**, *28*, 275705. [CrossRef] [PubMed]

23. Aminirastabi, H.; Xue, H.; Mitic, V.V.; Lazovic, G.; Ji, G.L.; Peng, D.L. Novel fractal analysis of nanograin growth in $BaTiO_3$ thin film. *Mater. Chem. Phys.* **2020**, *239*, 122261. [CrossRef]

24. Chen, Y.; Ye, H.H.; Wang, X.S.; Li, Y.X.; Yao, X. Grain size effects on the electric and mechanical properties of submicro $BaTiO_3$ ceramics. *J. Eur. Ceram. Soc.* **2020**, *40*, 391–400. [CrossRef]

25. Gu, L.L.; Li, T.; Xu, Y.J.; Sun, C.H.; Yang, Z.Y.; Zhu, D.L.; Chen, D.L. Effects of the Particle Size of $BaTiO_3$ Fillers on Fabrication and Dielectric Properties of $BaTiO_3$/Polymer/Al Films for Capacitor Energy-Storage Application. *Materials* **2019**, *12*, 439. [CrossRef]

26. Thanki, A.A.; Goyal, R.K. Study on effect of cubic- and tetragonal phased $BaTiO_3$ on the electrical and thermal properties of polymeric nanocomposites. *Mater. Chem. Phys.* **2016**, *183*, 447–456. [CrossRef]

27. Chen, T.; Meng, J.; Wu, S.; Pei, J.; Lin, Q.; Wei, X.; Li, J.; Zhang, Z. Room temperature synthesized $BaTiO_3$ for photocatalytic hydrogen evolution. *J. Alloys Compd.* **2018**, *754*, 184–189. [CrossRef]

28. Shmyt'ko, I.M.; Frolov, D.D.; Aronin, S.; Ganeeva, G.R.; Kedrov, V.V. Formation of new structural states in compressed $BaTiO_3$ nanopowders. *Phys. Solid State* **2017**, *59*, 1196–1205. [CrossRef]

29. Rotaru, R.; Peptu, C.; Samoila, P.; Harabagiu, V. Preparation of ferroelectric barium titanate through an energy effective solid state ultrasound assisted method. *J. Am. Ceram. Soc.* **2017**, *100*, 4511–4518. [CrossRef]

30. Sampaio, D.V.; Silva, M.S.; Souza, N.R.S.; Santos, J.C.A.; Rezende, M.V.S.; Silva, R.S. Electrical characterization of $BaTiO_3$ and $Ba_{0.77}Ca_{0.23}TiO_3$ ceramics It synthesized by the proteic sol-gel method. *Ceram. Int.* **2018**, *44*, 15526–15530. [CrossRef]

31. Zhang, X.T.; Cui, B.; Wang, J.; Jin, Q. The effect of a barium titanate xerogel precursor on the grain size and densification of fine-grained $BaTiO_3$ ceramics. *Ceram. Int.* **2019**, *45*, 10626–10632. [CrossRef]

32. Hongo, K.; Kurata, S.; Jomphoak, A.; Hayashi, K.; Maezono, R. Stabilization mechanism of the tetragonal structure in a hydrothermally synthesized $BaTiO_3$ nanocrystal. *Inorg. Chem.* **2018**, *57*, 5413–5419. [CrossRef] [PubMed]

33. Zhao, D.; Ying, D.; Hua, X.; Zhou, M. Preparation of size controllable $BaTiO_3$ nanoparticles in microemulsion at low temperature. *Adv. Mater. Res.* **2014**, *1004*, 63–68. [CrossRef]

34. Shut, V.N.; Mozzharov, S.E.; Bobrovskii, V.V. Effect of ultrasonic processing on the synthesis of barium titanyl oxalate and the characteristics of the $BaTiO_3$ powder prepared from it. *Inorg. Mater.* **2018**, *54*, 72–78. [CrossRef]

35. Li, J.; Inukai, K.; Takahashi, Y.; Tsuruta, A.; Shin, W. Formation mechanism and dispersion of pseudo-tetragonal $BaTiO_3$-PVP nanoparticles from different titanium precursors: $TiCl_4$ and TiO_2. *Materials* **2018**, *11*, 51. [CrossRef]

36. Grendal, O.G.; Blichfeld, A.B.; Skjaervo, S.L.; Bee, W.; Selbach, S.M.; Grande, T.; Einarsrud, M. Facile low temperature hydrothermal synthesis of $BaTiO_3$ nanoparticles studied by in situ X-ray diffraction. *Crystals* **2018**, *8*, 253. [CrossRef]

37. Zhao, P.; Wang, L.; Bian, L.; Xu, J.B.; Chang, A.; Xiong, X.; Xu, F.; Zhang, J. Growth mechanism, modified morphology and optical properties of coral-like $BaTiO_3$ architecture through CTAB assisted synthesis. *J. Mater. Sci. Technol.* **2015**, *31*, 223–228. [CrossRef]

38. Ozen, M.; Mertens, M.; Snijkers, F.; Cool, P. Hydrothermal synthesis and formation mechanism of tetragonal barium titanate in a highly concentrated alkaline solution. *Ceram. Int.* **2016**, *42*, 10967–10975. [CrossRef]

39. Gao, J.; Shi, H.; Yang, J.; Li, T.; Zhang, R.; Chen, D. Influencing factor investigation on dynamic hydrothermal growth of gapped hollow $BaTiO_3$ nanospheres. *Nanoscale Res. Lett.* **2015**, *10*, 1033. [CrossRef]

40. Xiong, X.; Tian, R.; Lin, X.; Chu, D.; Li, S. Formation and photocatalytic activity of $BaTiO_3$ nanocubes via hydrothermal process. *J. Nanomater.* **2015**, *2015*, 692182. [CrossRef]

41. Moghtada, A.; Moghaddam, A.H.; Ashiri, R. Tetragonality enhancement in $BaTiO_3$ by mechanical activation of the starting $BaCO_3$ and TiO_2 powders: Characterization of the contribution of the mechanical activation and postmilling calcination phenomena. *Int. J. Appl. Ceram. Technol.* **2018**, *15*, 1518–1531. [CrossRef]

42. Katsuki, H.; Furuta, S.; Komarneni, S. Semi-continuous and fast synthesis of nanophase cubic $BaTiO_3$ using a single-mode home-built microwave reactor. *Mater. Lett.* **2012**, *83*, 8–10. [CrossRef]

43. Yasui, K.; Kato, K. Numerical simulations of sonochemical production and oriented aggregation of $BaTiO_3$ nanocrystals. *Ultrason. Sonochem.* **2017**, *35*, 673–680. [CrossRef] [PubMed]

44. Xie, Y.C.; Wang, J.; Yu, Y.; Jiang, W.R.; Zhang, Z.C. Enhancing breakdown strength and energy storage performance of PVDF-based nanocomposites by adding exfoliated boron nitride. *Appl. Surf. Sci.* **2018**, *440*, 1150–1158. [CrossRef]

45. He, D.L.; Wang, Y.; Chen, X.Q.; Deng, Y. Core-shell structured $BaTiO_3@Al_2O_3$ nanoparticles in polymer composites for dielectric loss suppression and breakdown strength enhancement. *Compos. Part A Appl. Sci. Manuf.* **2017**, *93*, 137–143. [CrossRef]

46. Huang, Q.; Luo, H.; Chen, C.; Zhou, K.C.; Zhang, D. Improved energy density and dielectric properties of P(VDF-HFP) composites with TiO_2 nanowire clusters. *J. Electroceram.* **2018**, *40*, 65–71. [CrossRef]

47. Huang, Q.; Luo, H.; Chen, C.; Zhou, X.; Zhou, K.C.; Zhang, D. Enhanced energy density in P(VDF-HFP) nanocomposites with gradient dielectric fillers and interfacial polarization. *J. Alloys Compd.* **2017**, *696*, 1220–1227. [CrossRef]

48. Wang, J.C.; Long, Y.C.; Sun, Y.; Zhang, X.Q.; Yang, H.; Lin, B. Enhanced energy density and thermostability in polyimide nanocomposites containing core-shell structured $BaTiO_3@SiO_2$ nanofibers. *Appl. Surf. Sci.* **2017**, *426*, 437–445. [CrossRef]

49. Wang, J.C.; Long, Y.C.; Sun, Y.; Zhang, X.Q.; Yang, H.; Lin, B. Fabrication and enhanced dielectric properties of polyimide matrix composites with core-shell structured $CaCu_3Ti_4O_{12}$@TiO_2 nanofibers. *J. Mater. Sci. Mater. Electron.* **2018**, *29*, 7842–7850. [CrossRef]

50. Dai, Y.; Zhu, X. Improved dielectric properties and energy density of PVDF composites using PVP engineered BaTiO3 nanoparticles. *Korean J. Chem. Eng.* **2018**, *35*, 1570–1576. [CrossRef]